


## Efficient Charge Collection in Coplanar-Grid Radiation Detectors

J. Kunc,<sup>\*</sup> P. Praus, E. Belas, V. Dědič, J. Pekárek, and R. Grill

*Institute of Physics, Charles University in Prague, Faculty of Mathematics and Physics,  
Ke Karlovu 5, Prague 2, CZ-121 16, Czech Republic*

 (Received 2 February 2017; revised manuscript received 12 March 2018; published 14 May 2018)

We model laser-induced transient-current waveforms in radiation coplanar-grid detectors. Poisson's equation is solved by the finite-element method and currents induced by a photogenerated charge are obtained using the Shockley-Ramo theorem. The spectral response on a radiation flux is modeled by Monte Carlo simulations. We show a 10× improved spectral resolution of the coplanar-grid detector using differential signal sensing. We model the current waveform dependence on the doping, depletion width, diffusion, and detector shielding, and their mutual dependence is discussed in terms of detector optimization. The numerical simulations are successfully compared to experimental data, and further model simplifications are proposed. The space charge below electrodes and a nonhomogeneous electric field on a coplanar-grid anode are found to be the dominant contributions to laser-induced transient-current waveforms.

DOI: [10.1103/PhysRevApplied.9.054020](https://doi.org/10.1103/PhysRevApplied.9.054020)

### I. INTRODUCTION

High-energy radiation can be detected directly by converting photons into electrical signals or indirectly using scintillators and photodiodes. Direct conversion detectors are expected to have a higher signal-to-noise ratio and a higher spatial and temporal resolution, even on a single-photon-counting level. This could lead to spectrally resolved computed tomography applications and advanced medical x-ray imaging [1]. Efficient detector optimization is a challenging technological task. Single-crystal growth is one of them, a high mobility-lifetime product ( $\mu\tau$ ) is another one, and last but not least is the different mobility and trapping cross section of photogenerated holes. The latter one contributes to a significant degradation of the temporal resolution. A wide range of materials [1–4] provide good sensitivity; however, poor temporal performance is achieved. The low mobility of holes, compared to electron mobility, has been solved by coplanar-grid (CPG) detection [5] in CdZnTe detectors or by the semiconductor analogue of Frisch grids in gas ion chambers, also called virtual Frisch-grid detectors [6,7].

As the technology of the majority of proposed materials still needs to mature, the choice of GaAs, crystalline CdTe, or CdZnTe is mandatory for counting and high-energy-resolution applications. The problem with different electron and hole mobilities is overcome using the coplanar-grid electrodes, and it is proven also to be an efficient way to increase spectral resolution [8]. The coplanar-grid as well as other electron-only detection techniques [9,10] are

effective in overcoming some of the material problems of CdZnTe and, consequently, have led to efficient  $\gamma$ -ray detectors with good energy resolution while operating at room temperature [11].

Polarization effects and high-quality crystalline material remain as the main limitations. Their reduction has been addressed both experimentally and theoretically. Atomistic simulations [12,13] are a powerful method for exploring crystalline defects at a resolution unattainable by experimental techniques [14]. The determination of an electric-field shape precisely due to a relatively complicated electrode structure and the application of the bias and intergrid voltage simultaneously is also an experimentally difficult task. Though exact solutions are often tedious, simplified models have also been proposed. A small part of a pixel detector has been considered [15], and a spectral response has been modeled. Polarization and carrier trapping was solved by a simplified set of kinetic equations [16] in CdZnTe detectors, the effect of transport parameters' inhomogeneities (charge density, mobility, and potential fluctuations) and hot carriers were discussed [17], and plasmons in solid-state radiation detectors were studied [18]. The laser-induced transient-current technique (LTCT) provides information about charge-collection dynamics and detector polarization [19–22]. The major motivation for the LTCT, although not equivalent to the technologically important charge sensing, is to develop a convenient method to study a detector's internal electric field, an essential parameter for efficient charge collection and successive detector optimization. The internal electric field, giving information on the position and strength of the space charge, depletion width, and detector shielding efficiency,

<sup>\*</sup>kunc@karlov.mff.cuni.cz

is otherwise unattainable in charge-sensing detectors. The LTCT is used instead of a TCT due to the higher signal-to-noise ratio and simpler triggering, which is synchronized with a pulsed laser driver. The LTCT has been measured on pixel [1,23,24] and coplanar-grid detectors [25]. Though it is important for further detector optimization, the theoretical treatment is usually given only in simplified experimental geometries and the basic formulation of the Shockley-Ramo theorem [26]. The coplanar-grid detectors have also been modeled only in a simplified geometry, and a spectral response has been calculated [5,26–28]. Sparse realistic detector geometries were considered for x-ray spectra simulations [29,30]; however, no temporal response has been calculated.

We provide here an insight on carrier transport in a radiation coplanar-grid detector based on CdZnTe, valid also for other semiconductors used for direct conversion detector fabrication. We determine the influence of bulk semiconductor parameters on temporal and spectral resolution in a real detector geometry. The requirement on efficient charge collection is discussed with respect to the effects of the depletion width, diffusion, and detector shielding. The LTCT waveforms compared to the numerical model allow the evaluation of the electric-field profile inside the coplanar-grid detector with a high spatial resolution unattainable experimentally. The spectral-resolution improvement is quantitatively determined in a coplanar-grid detector, and the differential current sensing [5,27,31] is shown to overcome problems of low hole mobility, a high hole-trapping cross section, and the random nature of x- and  $\gamma$ -ray photon absorption within a detector. We also aim to show simplified analytically based considerations to understand the detector operation, which is useful for a qualitative optimization without the need of elaborate numerical calculations.

## II. METHODS

The LTCT response is modeled by the drift-transport mechanism of photogenerated carriers. The above band-gap photogeneration is assumed. Holes are neglected for their small mobility  $\mu_h \cong 100 \text{ cm}^2 \text{ V}^{-1} \text{ s}^{-1}$  and short lifetime [32]. For this reason, we assume electrons only [5] and collection times much shorter than an electron lifetime. In the LTCT, holes are swept to the cathode in subnanosecond times; hence, their influence is negligible. The current response caused by a moving charge between electrodes is calculated using the Shockley-Ramo theorem. The foundation of the Shockley-Ramo theorem is based on the known electrostatic potential in two cases. The first one consists of a real electrostatic potential distribution within a detector. The second is the potential distribution of a weighting potential. Here, the electrode of interest is biased to 1 V, and all other electrodes are at 0 V. The corresponding electric field determines the charge response on a given electrode, and the time derivative determines the current

response [33–36]. The full real potential and corresponding electric field determine the trajectory of photogenerated carriers. We assume only a small enough concentration of photogenerated carriers so that they do not spread by diffusion or electrostatic repulsion before reaching the anode. This is clearly fulfilled, since the diffusion-time broadening is about 15 ns and carriers take about 1  $\mu\text{s}$  from the cathode to the anode. The limitations of this assumption are discussed comparing the model and experimental data.

The LTCT current response is modeled by assuming a 2-mm-wide laser-spot size on the partially transparent cathode, and it is centered at the interception of the cathode and vertical axis of the detector. The axis intercepts the top of the detector right in the center between the collecting grid (CG) and noncollecting grid (NCG). We trace 300 electron trajectories equally spaced on a cathode center. The motion of each electron (electron packet) is calculated by integrating their drift velocity. The current response is then calculated for each of the 300 trajectories and summed up. The resulting summed current response is compared to experimental data. We also assume a positively charged depletion width below the cathode and a negatively charged space region below the anode, as commonly observed in a CPG. These space-charge regions give rise to a current decrease (increase) at the time of 0 (1  $\mu\text{s}$ ).

The experiments done by the hard x-ray and  $\gamma$ -ray transient-current technique (XTCT) are modeled by the solution of the Poisson equation, and, in the second computation step, electron trajectories are obtained by integrating their velocities (as in LTCT curves). However, here, the initial position of photogenerated carriers is determined in a Monte Carlo loop. The random position of photogenerated carriers is a model of the large absorption length of x- and  $\gamma$ -ray radiation; hence, the model holds for more than hundreds of eV energetic photons. Here, we do not sum all trajectories with a random initial position. Instead, the current response is calculated for each trajectory separately, and the total collected charge is calculated by integrating the current response in time. The electron-current response is considered only, since hole mobility is  $10\times$  lower [32] and holes have a higher trapping cross section. We trace 1500 trajectories, and the total collected charge from electron motion is statistically analyzed.

The electrostatic potential is calculated by solving Poisson's equation

$$-\Delta\varphi = \frac{\rho(\mathbf{r})}{\epsilon_0\epsilon_r} \quad (1)$$

by the finite-element method. The charge density  $\rho(\mathbf{r})$  is formed either by positively charged donors (donor density  $N_D$ ,  $\rho = eN_D$ ,  $e = +1.602 \times 10^{-19} \text{ C}$ ) in a depletion region at the cathode or by negatively charged acceptors (acceptor density  $N_A$ ,  $\rho = -eN_A$ ) in the depletion region at the anode. The permittivity  $\epsilon = \epsilon_r\epsilon_0$  is a product of the permittivity in vacuum  $\epsilon_0$  and relative permittivity of CZT

$\epsilon_r = 10$ . The boundary conditions are defined by an applied external bias between a cathode, CG, and NCG. The detector geometry is chosen to properly model a Redlen Inc. state-of-the-art CdZnTe CPG detector. The mesh triangulation is used to properly describe the size effects of the rectangular metal-anode grid. The anode behaves as a set of parallel charged wires when the charge is far from the anode compared to the anode characteristic size (anode strip width). And the anode behaves like an infinitely large planar electrode if the charge is close enough to the anode compared to the characteristic anode size. We consider the latter case as a measure of sufficiently dense triangulation. This regime can be analytically treated as well and pronounces itself as a constant electric field and linear-in-distance electrostatic potential.

The strong electric field at both electrodes causes velocity saturation. The field maximal values are approximately  $10^4$  V/cm, giving a drift speed up to  $1 \times 10^7$  cm/s assuming the electron mobility is  $\mu \approx 1000$  cm<sup>2</sup> V<sup>-1</sup> s<sup>-1</sup>. The saturation velocity in CdZnTe is about  $v_{\text{sat}} \approx 1 \times 10^7$  cm/s [37]; therefore, the velocity-field dependence is expected to show nonlinear behavior. The velocity saturation [38] is taken into account by

$$\mathbf{v}(\mathbf{r}) = \frac{\mu \mathbf{E}(\mathbf{r})}{\sqrt{1 + \left(\frac{\mu \mathbf{E}(\mathbf{r})}{v_{\text{sat}}}\right)^2}}, \quad (2)$$

where  $v(\mathbf{r})$  is the position ( $\mathbf{r}$ )-dependent drift velocity in electric field  $\mathbf{E}(\mathbf{r})$ . The electric field  $\mathbf{E}(\mathbf{r}) = -\nabla\varphi(\mathbf{r})$  is calculated from the total electrostatic potential  $\varphi(\mathbf{r})$ , which is the solution of the two-dimensional Poisson equation, as described above by Eq. (1). The electron's  $i$ th trajectory  $\mathbf{r}_i(t)$  is calculated as a time integral:

$$\mathbf{r}_i(t) - \mathbf{r}_i(0) = \int_0^t \mathbf{v}[\mathbf{r}(t')] dt' \quad (3)$$

of velocity  $v(\mathbf{r})$  with a boundary condition satisfying the initial position  $\mathbf{r}_i(0)$  of the electron motion at the cathode. The Shockley-Ramo theorem is used to calculate current response  $I_i^k$ :

$$I_i^k(t) \propto \mathbf{E}[\mathbf{r}_i(t)] \cdot \mathbf{E}_w[\mathbf{r}_i(t)] \quad (4)$$

on a given  $k$ th electrode, and it is proportional to the scalar product of actual electric field  $\mathbf{E}[\mathbf{r}_i(t)]$  in a detector and the weighting electric field  $\mathbf{E}_w[\mathbf{r}_i(t)]$  for the  $k$ th electrode along the trajectory of the  $i$ th electron. As the total measured current  $I^k$  is formed by all electrons, we sum over all electron trajectories:

$$I^k = \sum_{i=1}^N I_i^k. \quad (5)$$

The sum of all currents over all electrodes is zero, because there is no charge accumulation inside the detector. We calculate current  $I^{k,l}$  measured between the  $k$ th and  $l$ th electrodes as

$$I^{k,l} = I^k - I^l. \quad (6)$$

We assume here that the current flows from the  $l$ th electrode through the detector to the  $k$ th electrode.

### III. SAMPLES AND EXPERIMENTAL SETUP

The modeled LTCT waveforms are compared to experimental data measured on the coplanar-grid CdZnTe detector. The detector, purchased from Redlen Inc., has dimensions  $10 \times 10 \times 10$  mm<sup>3</sup>. The details of our LTCT setup [39,40] and data processing are described elsewhere [25]. The detector cathode is irradiated by optical pulses (approximately 3 ns as the FWHM, 200 ps rise and fall time) using the laser diode (660 nm, 300 mW) that is powered by an ultrafast pulse generator. The pulse output energy is 0.4 nJ, and the repetition rate is 100 Hz. A collimation and imaging optics and a translation stage is used in the setup to adjust the laser-diode beam onto the examined spot of approximately 3 mm<sup>2</sup> on the cathode. The neutral-density disk filter is placed in the beam line for optimal intensity attenuation of the laser pulse. Negative bias  $V_B$  is applied to the CPG detector cathode (up to  $-1700$  V), and supplementary intergrid voltage  $V_{\text{IG}}$  between the collecting and noncollecting anode grids is introduced by an additional adjustable low-noise voltage supply (0–200 V).

### IV. CHARGED IMPURITIES, DEPLETION WIDTH, AND DIFFUSION

The effect of doping is shown in Fig. 1 for positive space charge  $N_D = 0.7, 4.0, \text{ and } 16 \times 10^{10}$  cm<sup>-3</sup>. The current response in the LTCT is modeled for a CG in Figs. 1(a), 1(b), 1(e), and 1(f) and for a NCG in Figs. 1(c) and 1(d). The current response can be split into three characteristic intervals. The first one is given by charge deceleration in a positive space charge below the cathode. The second regime is at intermediate times when the charge moves through the part of the detector without any fixed space charge. The third regime is a time of charge collection at the anode. It can be seen from the numerical simulation that the peak current response at the collection time increases with decreasing doping. The initial current peak decreases with decreasing doping and ideally disappears. The initial current peak can give rise to a spurious signal contributing to a low-energy spectral shoulder in  $\gamma$ -ray spectra [7]. The anode intergrid bias is shown for two values 0 and 150 V in Figs. 1(a) and 1(c). We note that the intergrid bias does not influence the initial current response, as is shown in the inset in Fig. 1(e), in contrast to the cathode bias, the inset in Fig. 1(f). This is caused by the local effects of intergrid bias

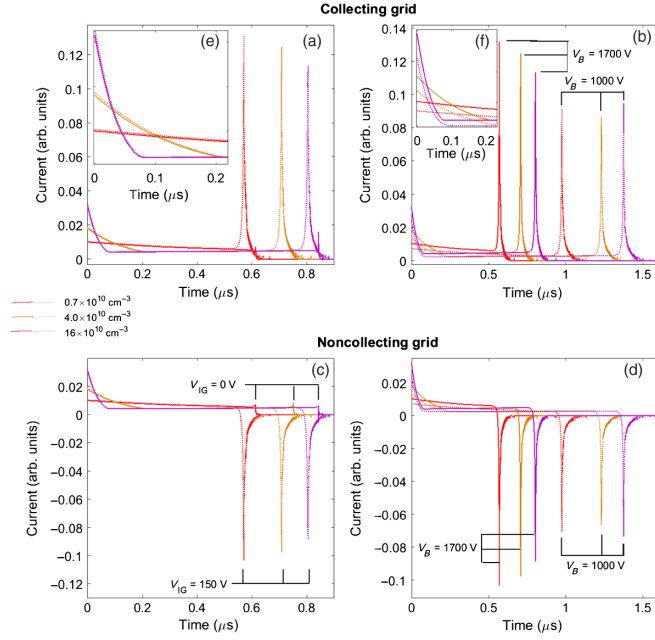


FIG. 1. Doping dependence of LTCT response curves. Doping densities  $N_D = 0.7, 4.0,$  and  $16.0 \times 10^{10} \text{ cm}^{-3}$  are distinguished by red, orange, and violet, respectively. Solid (dashed) curves in (a),(c),(e) show a numerical simulation for intergrid bias  $V_{IG} = 0 \text{ V}$  (150 V). Solid (dashed) curves in (b),(d),(f) show a numerical simulation for negative cathode bias  $V_B = 1700 \text{ V}$  (1000 V). The insets (e),(f) depict details of the current response around  $t \approx 0 \mu\text{s}$ . The space-charge width below the cathode is 0.64 DW. The simulation is shown for (a),(b),(e),(f) a collecting grid and (c),(d) a noncollecting grid. The  $V_{IG}$  trend (a),(c),(e) is studied for negative  $V_B = 1700 \text{ V}$ , and the  $V_B$  trend (b),(d),(f) is studied for  $V_{IG} = 150 \text{ V}$ .

on a small area around an anode. The cathode bias  $V_B$  (cathode to NCG bias) influences the mean field within a detector, thus, changing the current response for all times from the photocarrier generation to their complete collection on a CG.

The cathode depletion width dependence of the LTCT waveform is shown in Fig. 2. The cathode is a planar electrode, and the constant current is expected for the uncharged bulk semiconductor. The space charge (fixed or mobile) causes the deceleration of carriers, decreasing the current. The equilibrium depletion width (DW) is given by  $DW = \sqrt{[(2\epsilon V)/(qN_D)]}$ , where  $N_D$  is the doping density (or fixed space charge),  $V$  is a voltage drop within a depletion width, and  $\epsilon$  is the permittivity. The width of the depletion region varies from this simple model when carrier trapping and detrapping is assumed or more than one trapping level is located in the vicinity of the Fermi level. It can be seen from Fig. 2 that the peak current increases with a decreasing depletion width. This effect is due to the reduced total voltage drop in a depletion region and consequent higher voltage drop at the anode, the latter causing a higher electric field and higher current. We note

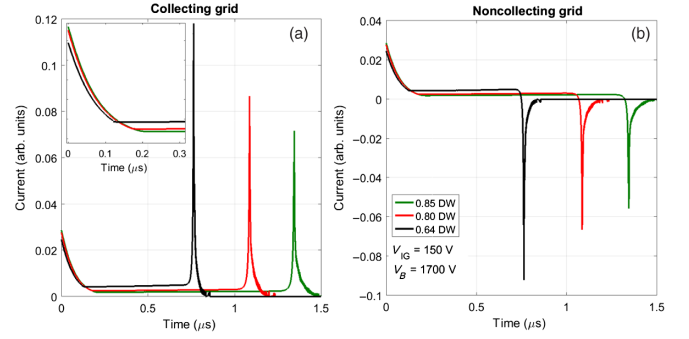


FIG. 2. Space-charge-width dependence of LTCT response curves. The space-charge width is measured in units of the equilibrium depletion width (DW) for  $N_D = 8 \times 10^{10} \text{ cm}^{-3}$ . The black, red, and green curves correspond to a depletion width of 0.64, 0.80, and 0.85 DW, respectively. The numerical simulation is shown for (a) a collecting and (b) a noncollecting grid. The inset in (a) depicts the detail of current evolution at  $t \approx 0 \mu\text{s}$ . The intergrid bias  $V_{IG} = 150 \text{ V}$  and cathode bias negative  $V_B = 1700 \text{ V}$ .

here that this is in contrast to doping density. The current response of a NCG is shown in Fig. 2(b). The current response is, similarly to a CG, stronger for a thinner depletion width.

The effect of diffusion is shown in Fig. 3. Diffusion takes an important role for long enough transit times  $t$  when temporal width  $\delta t$  caused by diffusion is comparable to or larger than the drift-current temporal width. For this reason, we show the current peak modification only at the charge collection at the anode. The temporal broadening (full width at half maximum) can be estimated from  $\delta t = 4\sqrt{D_e t \ln 2}/v$ , where  $D_e = \mu_e [(k_B T)/e]$  is the electron-diffusion constant related to electron mobility  $\mu_e$ , temperature  $T$ , and mean drift velocity  $v$ , which can be estimated from the transit time  $t$  and detector height  $d$ ;  $v = d/t$ . The current response for a CG and a NCG is shown for four diffusion broadening times (0, 10, 20, and

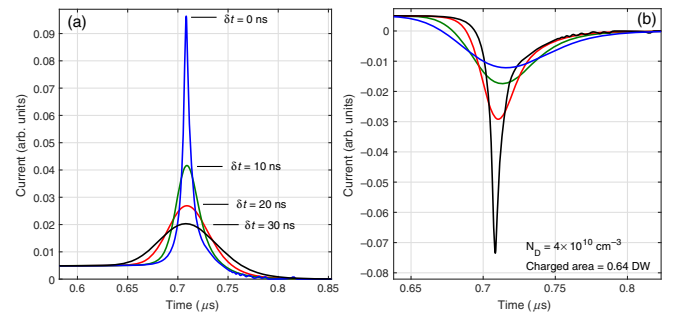


FIG. 3. The effect of diffusion on the LTCT current response; positive space charge below the cathode only (0.64 DW,  $N_D = 4 \times 10^{10} \text{ cm}^{-3}$ ). A diffusion peak broadening  $\delta t = 0, 10, 20,$  and  $30 \text{ ns}$  is assumed. The effect of diffusion is simulated for (a) a collecting and (b) a noncollecting grid. The intergrid bias  $V_{IG} = 150 \text{ V}$  and cathode bias  $V_B = 1700 \text{ V}$ .



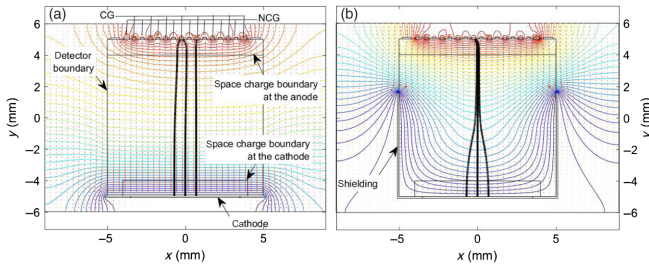


FIG. 4. Equipotential lines in (a) an unshielded and (b) a shielded detector. A detector area is depicted by thin solid black lines. The cathode is at 0 V (bottom planar contact), CG anode at negative 1850 V, and NCG anode at negative 1700 V (coplanar-grid anode at the top). Three representative electron trajectories are depicted as thick black lines.

30 ns). The current response is calculated for  $N_D = 4 \times 10^{10} \text{ cm}^{-3}$  and space-charge width 0.64 of the equilibrium depletion width.

## V. ELECTROSTATIC SHIELDING

Here, we study the effect of electrostatic shielding on the inner potential distribution within a detector. The detector shielding is assumed to cover 2/3 of the detector height. This coverage maximizes the shielding effect yet reduces a risk of material and surrounding air dielectric breakdown caused by the strong electric field between the cathode (top shielding edge) and anode. The critical electric field  $E_c = 3 \text{ kV/mm}$  in the air provides the possibility to apply  $V_{B,\text{max}} \approx 9 \text{ kV}$  between the shielded cathode and anode (shielding-anode gap 3 mm for 2/3 of detector height coverage). We show three trial electron trajectories in Fig. 4 for (a) an unshielded and (b) a shielded detector. The electron trajectories are almost parallel for the unshielded detector, and they tend to get localized to one trajectory in the shielded case. The current response is shown in Fig. 5. The initial current peak decreases to about 40% of the unshielded value, and the collection peak current rises by

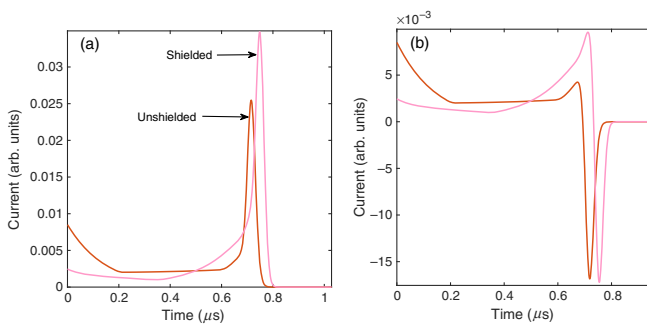


FIG. 5. The current waveform on a (a) CG and (b) NCG anode for an (orange) unshielded and a (light red) shielded detector. Calculated using the potential spatial distribution shown in Fig. 4.

approximately 30%. Both effects improve the detector functionality. The first peak reduction leads to a lower spurious signal and the stronger collection peak to a better signal-to-noise ratio.

## VI. EXPERIMENTAL DATA

The measured LTCT waveforms in a coplanar-grid detector on a CG and NCG anode are shown in Fig. 6. The data show good qualitative agreement (see Fig. 5), and in many aspects a quantitative comparison with simulated data can also be made, especially concerning the relative intensities of current peaks at the beginning and at the end of charge collection. The initially decreasing current is caused by decelerating electrons in a positive space charge below the cathode. The second collection current peak is stronger than the first one especially due to the strong electric field between the CG and NCG. This current also originates in a negative space charge below the anode. The current peak at the time of charge collection  $t \cong 700\text{--}800 \text{ ns}$  is broadened by electron diffusion. The amount of broadening estimated from the numerical simulation is  $\delta t \approx 10\text{--}12 \text{ ns}$ . The current peak at 0 ns is due to the temporal resolution of our oscilloscope (4 GHz bandwidth). The absorption occurs on a subnanosecond timescale, unattainable in our measurements; hence, we already see a well-developed current response of photogenerated free charge at 0 ns. The  $0.5 \mu\text{A}$  current peak at about 30–40 ns (Fig. 6) can be caused either by local inhomogeneity of the space charge below the cathode or due to electron-hole plasma dynamics in the first stages of their separation. Neither of these two effects is included in our model, and its origin will be a matter of our further work.

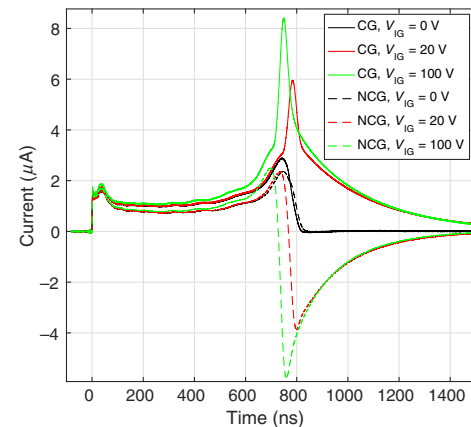


FIG. 6. Experimental data of the LTCT measured on a collecting grid (solid curves) and noncollecting grid (dashed curves) of a nonshielded detector for negative  $V_B = 1500 \text{ V}$  and three intergrid biases  $V_{IG} = 0, 20, \text{ and } 100 \text{ V}$  depicted by black, red, and green curves, respectively.

### VII. DIFFERENTIAL CURRENT SENSING

Here we study the importance of the measurement technique to detect photogenerated carriers. An example of three current waveforms detected on a CG, NCG, and differentially measured signal between a CG and NCG is shown in Fig. 7. The advantage of differential sensing is the lack of any signal before the charge reaches the coplanar-grid anode. There is no influence of the positive space charge at the cathode, since such a current response is equal for a CG and NCG. We note that the differential sensing does not bring a significant improvement for the LTCT, where the differential current waveform can be formed by data postprocessing, as is done in the numerical simulation in Fig. 7 to illustrate the method. The advantage is more pronounced when  $\gamma$ -ray photons are detected. Here, the absorption events occur randomly within a detector volume, and they contribute to signal broadening. The  $\gamma$ -ray photon detection is modeled in Fig. 8.

We trace 1500 trajectories of randomly generated photoexcited electrons [starting positions  $\mathbf{r}_i(0)$  in Eq. (3) are randomly chosen within the whole volume of the detector], and the total electron-induced charge is calculated. An example of 50 random trajectories is shown in Fig. 8(d). We note that, if holes are considered, the total collected charge is  $1e$ ; however, we assume a low hole mobility and high trapping cross section for holes. This leads to a much weaker current response or the current response on very long timescales in comparison to electron-induced TCT waveforms. For this reason, an electron traced from below the cathode gives a larger induced charge than electrons traced from the anode vicinity. The statistics of all Monte Carlo simulated absorption events are shown in Figs. 8(a)–8(c) for a CG, NCG, and differential sensing, respectively. The CG and NCG spectra of the collected charge have a rectangularlike shape caused by the equal

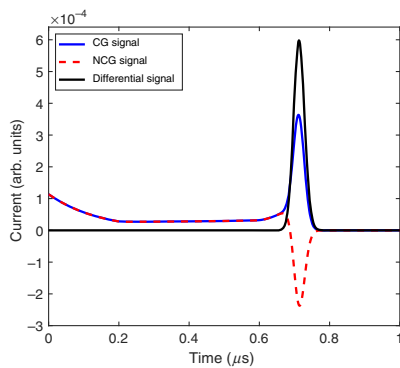


FIG. 7. LTCT current response for a  $V_B/3$  voltage drop at the cathode (positive space charge  $N_D = 4 \times 10^{10} \text{ cm}^{-3}$ ) and a  $V_B/10$  voltage drop at the anode (negative space charge  $N_A = 5 \times 10^{10} \text{ cm}^{-3}$ ). The current response is measured at the collecting grid (solid blue curve), noncollecting grid (dashed red curve), and differential signal (solid black curve). The applied biases are  $V_{IG} = 150 \text{ V}$  and negative  $V_B = 1700 \text{ V}$ .

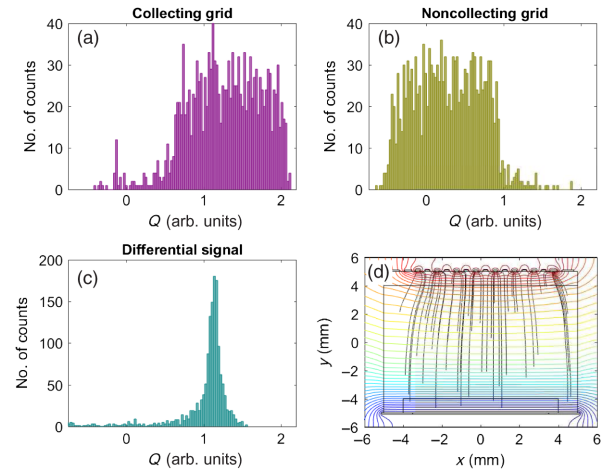


FIG. 8. Monte Carlo simulation of 1500 single  $\gamma$ -ray photon absorption events. The doping density, depletion widths, and applied biases are the same as in Fig. 7. The absorption probability is assumed to be equal throughout the detector volume. Currents induced by holes are neglected. The histograms (a)–(c) depict statistics of collected charge for all 1500 absorption events. The statistics are shown for the case of current measured on the (a) collecting and (b) noncollecting grid and (c) differential signal between collecting and noncollecting grids. Equipotential lines (blue to red contour lines), detector area (solid black lines), and 50 selected random absorption events are shown in (d).

distribution of absorption events within a detector. The mean collected charge on a NCG is shifted towards zero, because ideally no charge is collected by a NCG. We consider here a negative space charge at the anode. This space charge screens the electric field of the neutral bulk detector (no charge collected by the NCG), and it allows certain electron trajectories to be collected by the NCG.

In contrast to the CG current response, the differential sensing [see Fig. 8(c)] shows the same mean charge collection; however, the full width at half maximum is  $10\times$  smaller. This is caused by the signal insensitivity to the position of random-in-nature absorption events of  $\gamma$ -ray photons. We also note that there is no spurious signal at 0 ns (Fig. 7) caused by a positive space charge; hence, a reduced low-energy spectral shoulder [41] is expected beside the Compton scattering contribution. The effect of holes is also reduced regardless of the assumptions made in our simulations. Holes are attracted to the cathode, giving an even weaker response to a CG anode.

### VIII. DISCUSSION

General considerations to understand current waveforms follow from the Shockley-Ramo theorem  $i = eE_v v$ . A decreasing (increasing) current shows on a decreasing (increasing) electric field in a positive (negative) space charge at the cathode (anode). The space charge at the anode forms a weak current response at  $V_{IG} = 0 \text{ V}$ , and it causes a current shoulder for early times of charge

collection. The dominant signal at the charge collection time for  $V_{IG} > 0$  is caused by accelerated electrons in a spatially modulated electric field by intergrid bias  $V_{IG}$ . More specifically, we show that the cathode bias increases the peak current response. It also increases the initial signal caused by a positive space charge at the cathode, as shown in Fig. 1(b). This can lead to a spurious signal and to a low-energy spectral shoulder in x-ray spectra. At the same time, since the charge is swept faster through the detector bulk, there is a lower probability for carrier trapping and detector polarization. The lowest doping density is still the ultimate option here, because it worsens the charge collection efficiency. The effect of diffusion is twofold. First, the higher the diffusion or mobility, the faster the response time at a given detector size. Second, as absorption efficiency increases with the detector size, diffusion lowers the signal. Hence, for a fast response and strong current signal, a thinner detector is acceptable. We also point out that a thinner detector volume also eliminates carrier trapping. The optimal detector thickness and coplanar-grid dimensions can be established for differential signal sensing. The final peak width in the case of differential sensing is caused by a space charge at the anode, grid size (the signal increases for a denser anode grid), and carrier diffusion. A low diffusion rate also leads to a better signal-to-noise ratio. The diffusion length should be smaller than the anode intergrid spacing. If the diffusion length is comparable to or larger than the anode intergrid spacing, the CG and NCG diffusion-dominated current will be equal, and the differential signal will be negligible. Shielding is shown to improve the current waveforms in a solely drift model, as shown experimentally [42]. It improves the signal-to-noise ratio, decreases the initial spurious signal caused by a positive space charge at the cathode, and eliminates noise from the detector's external environment. Contrary to that, it slows the detector response time by about 5% and directs carriers into one single conducting channel inside the detector. The channeling effect leads to increased diffusion and electron repulsion even for intermediate times before charge collection.

As we do not assume charge trapping, it might be a source of error in our model. Recent Redlen CdZnTe detectors are distinguished by a mobility-lifetime product above  $0.01 \text{ cm}^2 \text{ V}^{-1}$ , which supplies the electron lifetime above  $10 \text{ } \mu\text{s}$ , assuming the electron mobility of about  $1000 \text{ cm}^2 \text{ V}^{-1} \text{ s}^{-1}$ . Correlating the lifetime with the electron transit time (approximately  $1 \text{ } \mu\text{s}$ ) from our experiments, the fraction of lost electrons may be estimated to less than 10%. The trapping can be eventually included by stochastically decreasing the number of electrons along their trajectories. This will result in an exponential time decrease of the current. However, as we experimentally observe rather a rising current, caused by an internal electric field, we conclude—also experimentally—that the trapping makes a minor contribution to the overall current waveform.

Next, further simplifications of the proposed numerical model are discussed. It is shown that many current waveform characteristics can be explained separately one by one using simple physical considerations. These are based on the electrostatic potential spatial distribution of the space charge in a bulk semiconductor and assuming a proper scaling of the charge-to-electrode distance. If the charge is close to the planar cathode with respect to the cathode dimension, the electric field can be considered constant. Then, the electrostatic potential linearly scales with the distance from the cathode. In the presence of a space charge below the cathode and charge-cathode proximity, the field scales linearly. The electrostatic potential scales quadratically with the charge-cathode distance in this case. The Shockley-Ramo theorem then gives the quadratic current waveform. The situation at the anode has to be split into two regimes. When the electron is far from the anode compared to the anode dimension, the electric field can be thought of as that of a charged wire. The intergrid potential difference will be negligible, and the electron effectively moves in the effective electric field given by the mean potential on the CG and NCG anode. This mean potential influences the transit time by the order of  $100D/L\%$ , where  $D$  is the anode width and  $L$  is a detector thickness. When an electron approaches an anode on a distance much smaller than the anode width, the situation becomes equal to the one at the cathode in close charge-cathode proximity. The iterative schemes can be applied to analytically describe field profiles through the whole detector volume. Deviations from these assumptions lead to other model parameters. We study a negative space charge below the anode as one example. We discuss diffusion due to localized carriers in one narrow potential minimum when shielding is applied as a second example of these deviations. The first additional parameter is easily taken into account in our drift model, and the second one exceeds our model limitations. The proper treatment of the latter case has to be solved by a coupled set of drift-diffusion, continuity, and Poisson equations. The numerical hardness of such a simulation, however, hinders the basic physical considerations as discussed above.

The mechanism of generating a charge in  $\gamma$ - or x-ray absorption and in the LTCT is different; however, the major difference (absorption of visible photon and  $\gamma$ -ray photon) is on a subnanosecond timescale, and it results in spatially localized nonequilibrium electron-hole plasma in either case. The main difference could be the behavior of such an electron-hole plasma if a different number of electron-hole pairs were to be generated. Since we are always in the low-density regime and at a high temperature (300 K), there is no expected transition to, e.g., an exciton or electron-hole liquid formation. We now estimate the number of photo- and  $\gamma$ - or x-ray-generated electron-hole pairs and compare their measured TCT signals. In the case of  $\gamma$ - and x-ray detectors, the photon energy is large enough (hundreds



of keV) to generate about  $10^4$ – $10^5$  electron-hole pairs (the electron affinity of CdTe is 4.4 eV). The number of photogenerated carriers can be estimated either from the intensity of laser light or directly from the LTCT. The first estimate, provided 0.4 nJ energy in a single laser pulse, a 660 nm excitation wavelength (1.88 eV), a cathode transmission of 1%, an illuminated area of  $1.5 \text{ mm}^2$ , and an absorption depth of  $1 \text{ }\mu\text{m}$ , results in  $4 \times 10^{12} \text{ cm}^{-3}$  dense plasma. The second estimate is based on an integrated charge approximately 1.5 pC from the LTCT current waveform (Fig. 6), giving a consistent estimate of  $3 \times 10^{12} \text{ cm}^{-3}$ . These densities lead to approximately  $10^7$  electron-hole pairs instead of  $10^4$ – $10^5$  in  $\gamma$ - or x-ray absorption; hence,  $\gamma$ - and x-ray absorption generates a  $10^2$ – $10^3$  smaller number of electron-hole pairs and accordingly a weaker TCT signal. We note that our experiments show that the  $\gamma$ - or x-ray TCT signal is about 2–3 orders of magnitude weaker than the LTCT (not shown here). The only issue is the so-called plasma effect if the laser intensity is too high. The equilibrium electron density in CdZnTe detectors is about  $1 \times 10^6 \text{ cm}^{-3}$ , which is 6 orders of magnitude less than the density of photogenerated carriers. These photogenerated carriers can screen the external electric field in the first few nanoseconds. This effect can slow down the detector response, and we always find such experimental conditions, by decreasing the laser intensity so the plasma effect is minimized. We also note that the plasma effect can also be beneficial to the study of alpha-particle absorption by the LTCT, since alpha-particle absorption can often be accompanied by the plasma effect. This regime of high electron-hole density might also be influenced by electron-hole recombination. The recombination process will affect the collected charge, and this is another reason why we carefully adjust experimental conditions so that we stay in the low-density regime where electron-hole recombination is negligible.

## IX. CONCLUSION

We provide a simple drift-based model to understand laser-induced transient-current waveforms. The model is compared to experimental data where a qualitatively full current waveform has been reproduced. The capability of the proposed model is shown to provide a quantitative agreement within limitations given mainly by diffusion and electron repulsion. We simplify the model even more based on our experience from the numerical simulations. The simplified analytical considerations are shown to provide fruitful insight into detector operation. The current waveforms are studied under varied doping density, positive and negative space charge, cathode and intergrid bias, diffusion length, and detector shielding. The trends on how current waveforms are influenced by these parameters provide numerical insight to a detector optimization. A mutual influence of these parameters is discussed, and their

possible contradiction is pointed out. Finally, we quantify the increased efficiency of the commonly employed differential sensing in hard x-ray and  $\gamma$ -ray detectors. A more elaborate extension of the work is discussed in terms of a nonlinear set of coupled drift-diffusion, continuity, and Poisson equations. The presented work is useful for quick insight into an advanced functionality of radiation detectors for the broad scientific community.

## ACKNOWLEDGMENTS

Financial support from the Technological Agency of the Czech Republic under Project No. TE01020445, the Grant Agency of the Czech Republic under Contract No. P102/16/23165S, and Grant Agency of Charles University under Grant No. 1170716 is gratefully acknowledged.

- 
- [1] Michael Overdick, Christian Baeumer, Klaus Juergen Engel, Johannes Fink, Christoph Herrmann, Hans Krueger, Matthias Simon, Roger Steadman, and Gnter Zeitler, Status of direct conversion detectors for medical imaging with x-rays, *IEEE Trans. Nucl. Sci.* **56**, 1800 (2009).
  - [2] Martin Nikl, Scintillation detectors for x-rays, *Meas. Sci. Technol.* **17**, R37 (2006).
  - [3] Safa Kasap, Joel B. Frey, George Belev, Olivier Tousignant, Habib Mani, Jonathan Greenspan, Luc Laperriere, Oleksandr Bubon, Alla Reznik, Giovanni DeCrescenzo, Karim S. Karim, and John A. Rowlands, Amorphous and polycrystalline photoconductors for direct conversion flat panel x-ray image sensors, *Sensors* **11**, 5112 (2011).
  - [4] D. Hampai, S. B. Dabagov, G. Della Ventura, F. Bellatreccia, M. Magi, F. Bonfigli, and R. M. Montereali, High-resolution x-ray imaging by polycapillary optics and lithium fluoride detectors combination, *Europhys. Lett.* **96**, 60010 (2011).
  - [5] P. N. Luke, Unipolar charge sensing with coplanar electrodes—Application to semiconductor-detectors, *IEEE Trans. Nucl. Sci.* **42**, 207 (1995).
  - [6] Aleksey E. Bolotnikov, Jamie Butcher, Giuseppe S. Camarda, Yonggang Cui, Gianluigi De Geronimo, Jack Fried, P. M. Fochuk, Anwar Hossain, Kihyun H. Kim, O. V. Kopach, G. Mahler, Matthew Marshall, B. McCall, Matthew Petryk, Emerson Vernon, Ge. Yang, and Ralph B. James, Design considerations and testing of virtual Frisch-grid CdZnTe detector arrays using the H3D asic, *IEEE Trans. Nucl. Sci.* **60**, 2875 (2013).
  - [7] A. E. Bolotnikov, K. Ackley, G. S. Camarda, C. Cherches, Y. Cui, G. De Geronimo, J. Fried, D. Hodges, A. Hossain, W. Lee, G. Mahler, M. Maritato, M. Petryk, U. Roy, C. Salwen, E. Vernon, G. Yang, and R. B. James, An array of virtual Frisch-grid CdZnTe detectors and a front-end application-specific integrated circuit for large-area position-sensitive gamma-ray cameras, *Rev. Sci. Instrum.* **86**, 073114 (2015).
  - [8] M. Amman and P. N. Luke, Optimization criteria for coplanar-grid detectors, *IEEE Trans. Nucl. Sci.* **46**, 205 (1999).
  - [9] Qiushi Zhang, Congzhe Zhang, Yanye Lu, Kun Yang, and Qiushi Ren, Progress in the development of CdZnTe



- unipolar detectors for different anode geometries and data corrections, *Sensors* **13**, 2447 (2013).
- [10] A. Owens, R. den Hartog, F. Quarati, V. Gostilo, V. Kondratjev, A. Loupilov, A. G. Kozorezov, J. K. Wigmore, A. Webb, and E. Welter, Hard x-ray response of a CdZnTe ring-drift detector, *J. Appl. Phys.* **102**, 054505 (2007).
- [11] M. Amman, J. S. Lee, and P. N. Luke, Electron trapping nonuniformity in high-pressure-Bridgman-grown CdZnTe, *J. Appl. Phys.* **92**, 3198 (2002).
- [12] D. K. Ward, X. W. Zhou, B. M. Wong, F. P. Doty, and J. A. Zimmerman, Analytical bond-order potential for the Cd-Zn-Te ternary system, *Phys. Rev. B* **86**, 245203 (2012).
- [13] D. K. Ward, X. W. Zhou, B. M. Wong, F. P. Doty, and J. A. Zimmerman, Analytical bond-order potential for the cadmium telluride binary system, *Phys. Rev. B* **85**, 115206 (2012).
- [14] A. Cola and I. Farella, Electric fields and dominant carrier transport mechanisms in CdTe Schottky detectors, *Appl. Phys. Lett.* **102**, 113502 (2013).
- [15] P. Guerra, A. Santos, and D. G. Darambara, An investigation of performance characteristics of a pixellated room-temperature semiconductor detector for medical imaging, *J. Phys. D* **42**, 175101 (2009).
- [16] Derek S. Bale and Csaba Szeles, Nature of polarization in wide-bandgap semiconductor detectors under high-flux irradiation: Application to semi-insulating  $\text{cd}_{1-x}\text{zn}_x\text{Te}$ , *Phys. Rev. B* **77**, 035205 (2008).
- [17] M. J. Harrison, D. S. McGregor, and F. P. Doty, Fano factor and nonuniformities affecting charge transport in semiconductors, *Phys. Rev. B* **77**, 195207 (2008).
- [18] T. C. Choy and A. M. Stoneham, Plasmon effects in solid-state radiation detectors, *Europhys. Lett.* **23**, 99 (1993).
- [19] C. Canali, F. Nava, and L. Reggiani, Drift velocity and diffusion-coefficients from time-of-flight measurements, *Top. Appl. Phys.* **58**, 87 (1985).
- [20] S. Uxa, E. Belas, R. Grill, P. Praus, and R. B. James, Determination of electric-field profile in CdTe and CdZnTe detectors using transient-current technique, *IEEE Trans. Nucl. Sci.* **59**, 2402 (2012).
- [21] K. Suzuki, T. Sawada, and K. Imai, Effect of dc bias field on the time-of-flight current waveforms of CdTe and CdZnTe detectors, *IEEE Trans. Nucl. Sci.* **58**, 1958 (2011).
- [22] A. Cola, I. Farella, and M. Anni an M. C. Martucci, Charge transients by variable wavelength optical pulses in CdTe nuclear detectors, *IEEE Trans. Nucl. Sci.* **59**, 1569 (2012).
- [23] Jae Cheon Kim, William R. Kaye, and Zhong He, Signal modeling of charge sharing effect in simple pixelated CdZnTe detector, *J. Korean Phys. Soc.* **64**, 1336 (2014).
- [24] Jae Cheon Kim, William R. Kaye, Hao Yang, Cassarah R. Brown, and Zhong He, Improvement of sub-pixel position sensing in nonuniform large-volume pixelated CdZnTe crystals, *IEEE Trans. Nucl. Sci.* **60**, 1201 (2013).
- [25] P. Praus, J. Kunc, E. Belas, J. Pekarek, and R. Grill, Charge transport in CdZnTe coplanar grid detectors examined by laser induced transient currents, *Appl. Phys. Lett.* **109**, 133502 (2016).
- [26] T. H. Prettyman, C. S. Cooper, P. N. Luke, P. A. Russo, M. Amman, and D. J. Mercer, Physics-based generation of gamma-ray response functions for CdZnTe detectors, *J. Radioanal. Nucl. Chem.* **233**, 257 (1998).
- [27] D. S. McGregor, Z. He, H. A. Seifert, D. K. Wehe, and R. A. Rojas, Single charge carrier type sensing with a parallel strip pseudo-Frisch-grid CdZnTe semiconductor radiation detector, *Appl. Phys. Lett.* **72**, 792 (1998).
- [28] A. G. Kozorezov, J. K. Wigmore, A. Owens, and A. Peacock, Theory of the dynamic response of a coplanar grid semiconductor detector, *Appl. Phys. Lett.* **91**, 023504 (2007).
- [29] Yuedong Ma, Shali Xiao, Guoqiang Yang, and Liuqiang Zhang, Design and study of a coplanar grid array CdZnTe detector for improved spatial resolution, *Appl. Radiat. Isot.* **94**, 314 (2014).
- [30] Lu Huang, Xingling Qu, Weiguang Yang, Dongmei Li, Yang Chen, Jing Jin, Linjun Wang, Wenqing Zhu, Weizhong Ding, and Weimin Shi, Simulation and characterization of polycrystalline mercuric iodide film detector based on coplanar grid electrode, *Vacuum* **122**, 54 (2015).
- [31] T. H. Prettyman, M. K. Smith, and S. E. Soldner, Design and characterization of cylindrical CdZnTe detectors with coplanar grids, *Proc. SPIE Int. Soc. Opt. Eng.* **3768**, 339 (1999).
- [32] J. Fink, H. Kruger, P. Lodomez, and N. Wermes, Characterization of charge collection in CdTe and CZT using the transient current technique, *Nucl. Instrum. Methods Phys. Res., Sect. A* **560**, 435 (2006).
- [33] W. Shockley, Currents to conductors induced by a moving point charge, *J. Appl. Phys.* **9**, 635 (1938).
- [34] Simon Ramo, Currents induced by electron motion, *Proc. IRE* **27**, 584 (1939).
- [35] G. Cavalleri, E. Gatti, E. Fabri, and V. Svetlo, Extension of Ramos theorem as applied to induced charge in semiconductor detectors, *Nucl. Instrum. Methods* **92**, 137 (1971).
- [36] Z. He, G. F. Knoll, D. K. Wehe, and Y. F. Du, Coplanar grid patterns and their effect on energy resolution of CdZnTe detectors, *Nucl. Instrum. Methods Phys. Res., Sect. A* **411**, 107 (1998).
- [37] A. Ruzin, Scaling effects in ohmic contacts on semiconductors, *J. Appl. Phys.* **117**, 164502 (2015).
- [38] S. Sze, *Physics of Semiconductor Devices* (Wiley, New York, 2007).
- [39] P. Praus, E. Belas, J. Bok, R. Grill, and J. Pekarek, Laser induced transient current pulse shape formation in (CdZn) Te detectors, *IEEE Trans. Nucl. Sci.* **63**, 246 (2016).
- [40] P. Praus, E. Belas, J. Franc, R. Grill, P. Hoschl, and J. Pekarek, Electronic pulse shape formation in transient charge and transient current detection approach in (CdZn) Te detectors, *IEEE Trans. Nucl. Sci.* **61**, 2333 (2014).
- [41] Agnese Giaz, Giulia Gosta, Franco Camera, Stefano Riboldi, Nives Blasi, Angela Bracco, Sergio Brambilla, and Benedicte Million, Measurement of  $\beta^-$ -decay continuum spectrum of  $^{138}\text{Ia}$ , *Europhys. Lett.* **110**, 42002 (2015).
- [42] Woo Jin Jo, Han Soo Kim, Jang Ho Ha, and Manhee Jeong, Optimization of shielding electrode lengths of virtual Frisch-grid CdZnTe radiation detector for gamma-ray detection, *Curr. Appl. Phys.* **15**, S51 (2015).